Title

Developmental, cellular, and biochemical basis of transparency in the glasswing butterfly *Greta oto*

Authors

Aaron F. Pomerantz[1,2*], Radwanul H. Siddique[3,4], Elizabeth I. Cash[5], Yuriko Kishi[6,7], Charline Pinna[8], Kasia Hammar[2], Doris Gomez[9], Marianne Elias[8], Nipam H. Patel[1,2,6*]

Affiliations

1. Department Integrative Biology, University of California Berkeley, Berkeley, CA 94720.
2. Marine Biological Laboratory, Woods Hole, MA 02543.
3. Image Sensor Lab, Samsung Semiconductor, Inc., 2 N Lake Ave. Ste. 240, Pasadena, CA 91101, USA.
4. Department of Medical Engineering, California Institute of Technology, Pasadena, CA 91125.
5. Department of Environmental Science, Policy, & Management University of California, Berkeley, Berkeley, CA 94720.
6. Department Molecular Cell Biology, University of California Berkeley, Berkeley, CA 94720.
7. Department of Biology and Biological Engineering, California Institute of Technology, Pasadena, CA.
8. ISYEB, 45 rue Buffon, CP50, Paris, CNRS, MNHN, Sorbonne Université, EPHE, Université des Antilles, France.
9. CEFE, 1919 route de Mende, Montpellier, CNRS, Univ Montpellier, Univ Paul Valéry Montpellier 3, EPHE, IRD, France.

*** Corresponding author**. Email: pomerantz_aaron@berkeley.edu, npatel@mbl.edu

Abstract (150 words)

Numerous species of Lepidoptera have transparent wings, which often possess scales of altered morphology and reduced size, and the presence of membrane surface nanostructures that dramatically reduce reflection. Optical properties and anti-reflective nanostructures have been characterized for several 'clearwing' Lepidoptera, but the developmental basis of wing transparency is unknown. We apply confocal and electron microscopy to create a developmental time-series in the glasswing butterfly, *Greta oto*, comparing transparent and non-transparent wing regions. We find that scale precursor cell density is reduced in transparent regions, and cytoskeletal organization differs between flat scales in opaque regions, and thin, bristle-like scales in transparent regions. We also reveal that sub-wavelength nanopillars on the wing membrane are wax-based, derive from wing epithelial cells and their associated microvillar projections, and demonstrate their role in enhancing-anti-reflective properties. These findings provide insight into morphogenesis of naturally organized micro- and nanostructures and may provide bioinspiration for new anti-reflective materials.

Introduction

The wings of butterflies and moths (Lepidoptera) have inspired studies across a variety of scientific fields, including evolutionary biology, ecology, and biophysics (*1–3*). Lepidopteran wings are generally covered with rows of flat, partially overlapping scales that endow the wings with colorful patterns. Adult scales are chitin-covered projections that serve as the unit of color for the wing. Each scale can generate color through pigmentation, which results from molecules that selectively absorb certain wavelengths of light, structural coloration, which results from light interacting with the physical nanoarchitecture of the scale, or a combination of both pigmentary and structural coloration *(4, 5)*. Cytoskeletal dynamics, including highly organized F-actin filaments during scale cell development, play essential roles in wing scale elongation and prefigure aspects of scale ultrastructure *(6, 7)*.

In contrast to typical colorful wings, numerous species of butterflies and moths possess transparent wings that allow light to pass through, so that objects behind them can be distinctly seen (Fig. 1A-H, *8–10*). This trait has been interpreted as an adaptation in the context of camouflage, in which some lineages evolved transparent wings as crypsis to reduce predation (*11–13*). Transparency results from the transmission of light across the visible spectrum through a material, in this case the chitin membrane, without appreciable absorption or reflection. Levels of reflection are largely determined by the differences in refractive indices between biological tissues and the medium, and a larger difference results in higher surface reflection. Previous studies on transparency in nature have focused primarily on aquatic organisms, which are frequently transparent, aided by the close match between the refractive indices of their aqueous tissue and the surrounding media — water (*14*). By contrast, transparency is rare and more challenging to achieve on land, primarily due to the large difference between the refractive indices of terrestrial

organism's tissue (n = ~1.3-1.5) and air (n = 1), which results in significant surface reflection (*9, 15, 16*).

Nevertheless, some organisms have evolved morphological innovations that overcome the challenges of terrestrial transparency, notably in the form of anti-reflective nanostructures. Early studies elucidated highly-ordered sub-wavelength nanostructures (termed 'nipple arrays') on the corneal surface of insect eyes (*17*). These structures were found to generally be ~150-250 nm in height and spaced ~200 nm apart, which reduces reflection across a broad range of wavelengths by creating a smoother gradient of refractive indices between air and chitin (*18*). Nanostructure arrays have also been identified on the wings of cicadas, which helps to reduce surface reflection over the visible spectrum (*19*).

Some lepidopterans possess modified wing scales that allow light to reach the wing surface, which is composed of chitin and has some inherent transparency, but due to the high refractive index of chitin, n = 1.56 (*20*), the wing surface reflects light. For example, the butterfly *Methona confusa* (Nymphalidae: Ithomiini) has exposed wing membrane that lacks nanostructures on the surface, and as a result, the wing is somewhat transparent, but retains a high degree of reflectivity (for example, see Fig. 1A-C). Conversely, the longtail glasswing, *Chorinea faunus* (Riodinidae), was found to contain small, widely spaced scales and dome-shaped chitin nanoprotuberances on the membrane that generate anti-reflective properties (Fig. 1D-F) (*21*). The hawkmoth, *Cephonodes hylas* (Sphingidae), has nude wings due to its scales falling out upon eclosion, and was found to possess anti-reflective nanostructures on its wing surface that morphologically resemble insect corneal nipple arrays (9). Nipple array nanostructures have also been characterized in transparent wing regions of the tiger moth *Cacostatia ossa* (Erebidae) (*22*). Finally, the glasswing butterfly *Greta oto* (Nymphalidae: Ithomiini) was found to contain thin,

vertically oriented scales, allowing the wing surface to be exposed, along with nanopillars that coat the surface. These irregularly arranged nanopillars feature a random height and width distribution and were found to enable omnidirectional anti-reflective properties (Fig. 1G-I) (*10, 23*). More recent studies have explored aspects of structural diversity, optical properties, phylogenetic distribution, and ecological relevance of transparency within a wide range of butterflies and moths, highlighting that transparency has evolved multiple times independently and may present evolutionary benefits (*13, 24*).

Lepidoptera are proving to represent an excellent group to investigate transparency on land, but the developmental processes underlying wing transparency are currently unknown. This presents a gap in our understanding of lepidopteran wing evolution and diversification, as transparent butterflies and moths contain multitudes of intriguing scale modifications and sub-wavelength cuticular nanostructures (*24*). We therefore set out to explore the development of wing transparency in the glasswing butterfly *Greta oto,* which belongs to a diverse tribe (~393 species) of predominantly transparent neotropical butterflies (*25*). We applied confocal and transmission electron microscopy to compare wing development, scale cytoskeletal organization, and membrane surface nanostructures between clear and opaque wing regions. Using chemical treatments, scanning electron microscopy, and gas chromatography–mass spectrometry, we found that nanostructures on the wing membrane surface are made of two layers: a lower layer of chitin-based nipple-like nanostructures, and an upper layer of wax-based nanopillars composed predominantly of long-chain *n*-alkanes. Finally, by removing the wax-based nanopillars, we demonstrate their role in dramatically reducing reflection on the wing surface via optical spectroscopy and analytical simulations.

117 **Results**

118 **Scale measurements in clear and opaque wing regions of adult *Greta oto***

119 We investigated features of scale density, scale morphology, and the amount of wing
120 surface exposed in wings of adult *Greta oto*. We focused on two adjacent regions within
121 the forewing for consistency: a clear region within the discal cell and an opaque region
122 that consists mainly of black scales near the M2-M3 crossvein. (Fig 1G,J). The clear wing
123 region contained two types of alternating scale morphologies: bristle-like scales and
124 narrow, forked scales, while within the opaque wing region, scale morphologies
125 resembled 'typical' butterfly pigmented scales: flat and ovoid with serrations at the tips
126 (Fig1. K,L). The mean density of scales (± SD) in the adult wing were significantly lower
127 within the clear region (107 ± 19 scales per mm^2) compared to the opaque region (395 ±
128 23 scales per mm^2) (Student's t-test, $P < 0.001$, n = 3 individuals, Fig. 1M). In the clear
129 region, forked scales were significantly smaller in size (498 ± 39 μm^2) compared to the
130 bristle-like scales (831 ± 183 μm^2), while in the opaque region, scales were the largest
131 (3467 ± 382 μm^2) (ANOVA test, n = 3 individuals, Fig. 1N). Finally, the amount of
132 exposed wing membrane was significantly different between wing regions, with an
133 average of 83.1% ± 0.76 and 2.4% ± 3.4 exposed membrane in the clear and opaque
134 regions, respectively (Student's t-test, $P < 0.001$, n = 3 individuals, Fig. 1O).

135

136 **Morphogenesis and cytoskeletal organization of developing scale cells**

137 To investigate developmental processes of wing and scale development, we performed
138 dissections of *G. oto* pupae at different time points (Fig. 2). As in other species of
139 Lepidoptera, the early pupal wing consisted of a thin bilayer of uniform epithelial tissue
140 and by 16 hours after pupal formation (APF) numerous epidermal cells had differentiated
141 to produce sensory organ precursor (SOP) cells, which could be identified by fluorescently

142 labelling tissue with DAPI (Fig. 2B,C) as the SOP's are larger than, and positioned
143 slightly basal to, the rest of the epidermal cells. The SOPs are precursors to the scale and
144 socket cells and are organized into parallel rows. At this early stage of wing development,
145 we observed that the clear wing region harbored a lower density of SOP cells relative to
146 the opaque wing region (Fig. 2B,C). We can therefore infer that early into wing
147 development, SOP cell patterning is differentially regulated between clear and opaque
148 regions, which impacts the adult wing scale density and the amount of wing membrane
149 surface exposed in different parts of the wing.

150 Next, we investigated cellular and cytoskeletal organization during scale growth in
151 clear and opaque wing regions, using simultaneous confocal imaging of fluorescently
152 labeled scale cell membrane (wheat germ agglutinin; WGA), and F-actin (phalloidin) (Fig.
153 2D-I). We found that general aspects of scale development in *G. oto* follow those
154 previously reported in several butterfly and moth species by *(6)*, with some notable
155 distinctions for modified scale growth in the clear wing regions of *G. oto*.

156 By 30 hours APF, the SOP cells have divided to produce the scale and socket cells
157 (Fig. 2D,E). The scale cell body lies internally within the wing, while the socket cell
158 associated with each scale cell lies in a more superficial position. At this pupal stage, the
159 morphological development of wing scale projections has begun, and the scale cells
160 develop as small buds containing short, densely packed parallel F-actin filaments.
161 Phalloidin staining showed the appearance of these small cylindrical buds containing F-
162 actin filaments, and WGA staining showed outlines of the membrane as the scale
163 outgrowths begin to project and elongate beyond the wing surface. At this stage, budding
164 scales in the clear wing region appeared morphologically similar to the unspecialized
165 opaque scales: roughly elongated balloon-shaped with numerous small actin rods fanning
166 out from the pedicel to the apical tip of the scale. In the clear region, early scale

167 projections showed alternating sizes. In the opaque region similar budding scales at a
168 higher density were found, with larger buds corresponding to future cover scales, and
169 smaller, shorter buds corresponding to future ground scales (Fig. 2D,E).

170 By 48 hours APF, scale cell extensions have grown and elongated (Fig. 2F,G). The
171 actin filaments have reorganized into smaller numbers of thick, regularly spaced bundles
172 along the proximal–distal axis of the scale just under the surface of the cell membrane. At
173 the base of the scales, fluorescent staining indicated that F-actin bundles are tightly
174 packed, while in more distal regions we could see an asymmetric distribution of F-actin,
175 with larger actin bundles in the adwing (facing the wing membrane) side of the scales
176 (movie S1). At this stage, scales in different regions of the wing had also started to take on
177 dramatically different morphologies. Scales in the clear region had elongated in a vertical
178 orientation and obtained two types of alternating morphologies: short and triangular, or
179 long and bristle-like outgrowths (Fig. 2F). The wings of other butterfly species contain
180 alternating ground and cover scales, in which the ground scales are typically smaller in
181 size than the cover scales, consistent with our observations of the opaque regions of *G. oto*
182 (Fig. 2F). Based on scale size and position, we interpret that within the clear wing region
183 of glasswing butterflies, the larger bristle-like scales are modified cover scales and smaller
184 forked scales are modified ground scales (Fig. 2F). In the opaque region, scales have taken
185 on a round and flattened morphology, similar to what has been described in other colorful
186 butterfly and moth species, with the ground scales being shorter and wider than the cover
187 scales (Fig. 2G).

188 By 60 hours APF, scale projections have become even more elongated (Fig. 2H,I).
189 The triangular scales in the clear wing region have proceeded to generate two new
190 branches, which fork and elongate at the tips bidirectionally, while bristle-like scales have
191 elongated and curved (Fig. 2H). In the opaque region, scales were longer, wider, flatter,

192 and had developed serrations at the tips (Fig. 2I). F-actin bundles extended all the way to
193 the distal tips of these serrations, which has been shown to be necessary to produce finger-
194 like projections at the tips of scales (*6*). Phalloidin staining also revealed that actin bundles
195 were arranged in more symmetrical patterns around the periphery of the bristle-like scale
196 morphologies, forked scales showed modified actin organization at the branching points,
197 and actin bundle asymmetry was greatest in developing flat opaque scales, with larger
198 bundles present on the adwing side (Fig. 2H,I).

199 **Ultrastructure analysis of developing bristle, forked and opaque scales**

200 To reveal ultrastructural detail of developing wing scale morphology, we performed
201 transmission electron microscopy (TEM) on pupal wing tissue of *G. oto* at 48 hours APF
202 (Fig. 3). In transverse sections, we could resolve distinct scale morphologies (bristle,
203 forked and opaque) and their associated cytoskeletal elements.

204 Bristle-like scales in the clear wing regions were circular in cross sections (Fig.
205 3A-C). We could also distinguish between distal and basal regions of bristle-like scales,
206 the latter of which had the presence of a surrounding socket cell in the cross section (Fig.
207 3B,C). TEM revealed that these bristle-like scales were ringed by peripheral bundles of
208 actin filaments, which lay spaced just under the cell membrane (Fig. 3B-C'). On the
209 adwing side of the scale, the actin bundles were larger and spaced closer to one another
210 relative to the abwing side, and in more distal regions of the bristle-like scale, the actin
211 bundles were more widely spaced and smaller in size. We also observed large populations
212 of microtubules (MTs) distributed throughout the developing scales, which were internal
213 relative to the actin bundles. Interestingly, we observed different patterns of microtubule
214 distribution within different developing scale morphologies. The cross section of bristle-
215 like scales revealed large populations of internal microtubules, which we identified due to
216 their characteristic ring shape and diameter of ~25 nm (Fig. 3B',C'). The circular ring

217 shape of microtubules in cross sections of both the basal and distal parts of the bristle-like
218 scale suggested that microtubules are all longitudinally oriented, running in the same
219 direction as the actin filaments, parallel to growth. We also observed that populations of
220 MTs are localized primarily away from the surface of the scale in its interior, and MTs
221 were fewer distally than basally (Fig. 3B',C').

222 In our TEM cross sections we also observed scale types that appeared more
223 triangular in shape, suggesting that these corresponded to developing forked scales within
224 the clear wing region (Fig. 3D,E). We observed that these scales were ringed by peripheral
225 bundles of crosslinked actin filaments, with thicker actin bundles on the adwing side of the
226 scale. Interestingly, we observed two internal bundles of actin filaments that were not
227 observed in bristle-like scale morphologies (Fig. 3E'). We also note that there was
228 variability in MT orientation, rather than the ubiquitous longitudinal orientations observed
229 in bristle-like scales.

230 Finally, developing opaque scales were easily identified in cross sections due to
231 their large size and flattened morphology (Fig. 3F,G). We observed peripheral bundles of
232 crosslinked actin filaments that were widely spaced and smaller in size in distal parts of
233 the scale (Fig. 3G-G'). We observed a clear asymmetry in actin bundle size, which were
234 thicker on the adwing side of the scale relative to the abwing surface. In opaque wing
235 regions, TEM micrographs revealed what appeared to be concentrated parallel-running
236 populations of MTs near the narrow base of the scales, and then a more mesh-like network
237 of MTs in more distal flattened regions, indicating that MTs have varying orientations
238 within different regions of the scale (Fig. 3G,G', fig. S1). In contrast to the bristle-like
239 scales, large, flattened opaque scales appeared to contain populations of MTs that were
240 more widely distributed and less dense.

241 In all scale types we observed the presence of numerous internal organelles and
242 vesicles, including mitochondria, electron dense vesicles and free ribosomes (Fig. 3, fig.
243 S1). We also observed that the actin bundles contained dense, hexagonally packed F-actin
244 filaments, supporting previous patterns for actin bundle formation in elongating insect
245 scales (fig. S1). The neck regions of different scale morphologies were predominantly
246 filled with longitudinally oriented microtubules, actin bundles, and mitochondria.
247 Longitudinal views also supported that MTs are numerous in the outgrowing scale, and
248 their spatial arrangement differed with scale position and shape. More mature scales
249 around 120 hours APF exhibited developed ridge morphologies and thickened cuticle
250 layers (fig. S1).

251 **Ontogeny of wing membrane nanostructures**

252 The clear wing regions of *G. oto* contain nanopillars that cover the surface of the
253 membrane (Fig 1I, Fig 4A). These nanopillars were previously characterized in adult
254 wings, which feature an irregular height distribution and help to generate omnidirectional
255 anti-reflective properties (*10*). In order to gain insight into the development of these
256 nanostructures, we examined the surface of the wing membrane epithelial cells with TEM
257 (Fig. 4B-F). At 60 hours APF, a perpendicular section through the wing epithelia showed
258 a continuous epithelial lamina (Fig. 4B,C). We observed the epithelial cells contained
259 microvilli (MV), which appeared as slender linear extensions from the inner margins of
260 the developing cells that insert into electron-dense material (Fig. 4B,C). The surface layer
261 of the epithelia appeared as an extracellular lamellar system, and lamina evaginations
262 appeared in the section as domes distal to the microvillar extensions (Fig. 4C). By 72
263 hours APF, we observed a thin outer layer of the epicuticle that rose above the epidermal
264 cells and by 120 hours APF, we found that this upper layer above the microvilli
265 contained what appear to be dome-shaped protrusions and thickened cuticle, possibly

266 secreted from regularly spaced microvilli (Fig. 4D,E). Finally, in our TEM cross section
267 of a fully developed adult wing of *G. oto*, we observed that the membrane surface
268 harbors dome-shaped nanoprotrusions with similar morphologies to insect corneal
269 surface nipple arrays (e.g. *9, 17*), which we refer to throughout the text now as "nipple
270 nanostructures", and an upper layer containing pillar-like protrusions, which we refer to
271 as "nanopillars", that featured a more irregular height distribution (Fig. 4F). These
272 results show early subcellular processes of developing nanopillars within the clear wing
273 region, which arise distal to microvillar extension in epithelial cells.

274 **Topographical organization and biochemical composition of wing surface**
275 **nanostructures**

276 Based on our EM results of membrane nanostructures, we set out to investigate the
277 topographical organization and biochemical composition of the adult wing surface. To do
278 so, we treated individual, disarticulated adult *G. oto* wings in two ways: by 1) physically
279 removing wing surface nanostructures by gently pressing and rubbing a wing in between
280 paper and Styrofoam (after *9*) and 2) testing the wing surface structures for solubility in
281 organic solvents, including hexane and chloroform to extract lipids (after *26*). We then
282 performed SEM to compare wing surface topography of untreated and treated wing
283 samples (Fig. 5A-C'). SEM confirmed that the first treatment partially or completely
284 removed nanostructures across the wing membrane surface (Fig. 5B). In a region of partial
285 removal, we could identify smaller, dome-shaped nipple nanostructures underneath the
286 top layer of nanopillars (Fig. 5B'). SEM of the chemically treated wing surface revealed
287 that the upper layer of irregularly sized nanopillars were completely removed, revealing a
288 layer of regularly arranged dome-shaped nipple nanostructures that did not dissolve
289 through chloroform or hexane exposure (Fig. 5C,C'). Therefore, we hypothesized that the

290 upper layer of irregularly sized nanopillars consisted of a secreted wax-based material,
291 which sits above smaller chitin-based nipple nanostructures.

292 To test this hypothesis, we extracted the surface layer of *G. oto* clear wing regions
293 with either hexane or chloroform and analyzed the chemical composition by gas
294 chromatography–mass spectrometry (GC-MS). We found that the chemical profile
295 generated by both hexane and chloroform extracts yielded similar results (Fig. 5D). In all
296 extracts, we identified two straight-chain alkanes that made up approximately 2/3 of the
297 compounds detected: 41.64 ± 5.75% pentacosane ($C_{25}H_{52}$) and 23.32 ± 5.35% heptacosane
298 ($C_{27}H_{56}$) (Table S1). The remaining compounds were primarily composed of slightly larger
299 methyl-branched alkanes (monomethyl and dimethyl C27, C29 and C31) and esters.
300 Therefore, our results suggest that in *G. oto* there are two components to wing surface
301 ultrastructure: procuticle-based nipple nanostructures, and an upper epicuticular layer of
302 irregularly sized nanopillars, composed mainly of straight chain alkanes (Fig. 5D,E).

303 **Anti-reflective properties of wax-based nanopillars**

304 To test whether the wax-based nanopillars play a role in wing reflection, we measured the
305 reflectance spectra of untreated and hexane-treated wings (Fig. 6). Additionally, we
306 measured nanostructure geometries and membrane thickness from wing SEM cross
307 sections (n = 6), and determined the average distance between two nanostructures as d =
308 174 nm, conical shaped cuticular nipple nanostructures height, h_p = 77 nm, wax-based
309 irregular nanopillars radius, r_{np} = 53 nm, mean height, h_{np} = 224 nm and variance σ_{np} =
310 49.3 nm, and membrane thickness, h_m = 746 nm and variance σ_m = 43 nm (Fig. 6B,D, fig.
311 S2). On the basis of SEM micrographs for treated and untreated samples, we modeled
312 three wing architectures consisting of 1) nanopillars with variable height together with
313 cuticle-based nipple nanostructures on the wing membrane, 2) cuticle-based nipple
314 nanostructures on wing membrane and 3) wing membrane without any nanostructures, to

315 simulate the optical properties for different conditions (Fig. 6E). The simulated reflectance
316 data of the untreated and treated conditions in Fig. 6F closely resembled the experimental
317 ones. In untreated wings of *G. oto*, we found that transparent regions have a low total
318 diffuse reflection of about 2%, which is in line with previous reflectance measurements of
319 this species (Fig. 6F, *10*). By contrast, the hexane treated wings without the upper layer of
320 wax nanopillars had about 2.5 times greater reflectance relative to the untreated wings,
321 and generated an iridescent thin film spectra, even though they harbored dome-shaped
322 nipple nanostructures (Fig. 6D,F).

323 For simulated data, the overall reflectance ratio of the hexane treated wing to that
324 of the untreated was approximately three, similar to experimental reflectance data (Fig.
325 6F, Table S2). Most importantly, the simulated results for the untreated wing with wax-
326 based irregular nanopillars make reflectance more uniform across wavelengths, which
327 reduces the iridescent effect of the wing membrane. Finally, we simulated a thin film
328 membrane without any nanostructures, which showed reflectance (averaged from all
329 wavelengths) of the membrane itself to be 8.81 ± 3.46%, whereas the treated and untreated
330 wing reflections were 5.78 ± 2.82% and 1.93 ± 0.77%, respectively (Fig. 6F). While
331 treated wings harboring dome-shaped nipple nanostructures reduced the overall
332 reflectance relative to the membrane only, their effect was not strong enough to reduce
333 reflectance spectra oscillation. The wax-based irregular nanopillars on top introduced a
334 more gradual transition between refractive indices to lessen the oscillation by
335 approximately five-fold, in addition to reducing overall reflection (Fig, 6F). Additionally,
336 we simulated the three wing architecture models considering different mean membrane
337 thicknesses and variance in membrane thickness (fig. S3). We found that variance in wing
338 membrane thickness reduced reflectance spectra oscillations, rather than mean membrane
339 thickness alone, and more peaks appear in the visible spectrum with increasing thickness

340 of the membrane. (fig. S3, Table S3). Overall, these results demonstrate that the non-
341 constant architecture of the wing membrane and wax-based irregular nanopillars on the
342 wing surface of *G. oto* function to dramatically enhance anti-reflective properties.

343 **Discussion**

344 Butterflies and moths have evolved sub-wavelength anti-reflective structural innovations
345 that enable them to be transparent, which is rare amongst terrestrial organisms. Here we
346 report the details of pupal wing development and cytoskeletal organization in the
347 glasswing butterfly, *Greta oto*, as well as insights into the ontogeny and biochemical basis
348 of wing surface nanostructures that reduce reflection.

349 The arrangement of unicellular projections in insect integument, such as bristles
350 and scales, has been a model for research on cellular pattern formation (*27*). Shortly after
351 pupation, sensory organ precursor (SOP) cells develop from a monolayer of epithelial
352 cells into orderly arrangements, then differentiate into scale and socket cells. In the present
353 study, we found that early SOP cell patterning impacts the final adult scale density in *G.*
354 *oto* and this feature of spacing scale cells farther apart, and therefore reducing the overall
355 density of scales, is an initial step to generate clear wings. One study showed that during
356 early pupal development, the receptor molecule Notch is expressed in a grid-like pattern in
357 the wing epithelium (*28*). This may contribute to the parallel rows of uniformly spaced
358 SOP cells that express low levels of Notch, likely through a lateral inhibition mechanism.
359 Previous work has shown that the low-Notch SOP cells express a homolog of the *achaete-*
360 *scute* proneural transcription factors, which likely plays a role in scale precursor cell
361 differentiation (*29*). Notch-mediated lateral inhibition could establish a dense population
362 of ordered SOP cells in the developing wing, resulting in a characteristic ratio of scale-
363 building and epithelial cells. It would be interesting for future studies to investigate if

364 modifications in Notch signaling play a role in scale cell patterning in clearwing
365 butterflies and moths, many of which contain reduced densities of scale cells (*24*).
366 The range of morphological diversity among scales and bristles within Lepidoptera
367 likely results from components or modifiers of the cytoskeletal structures and cell
368 membrane. One study surveyed a wide range of developing butterfly and moth scales and
369 identified that F-actin is required for several aspects of scale development, including scale
370 cell elongation and proper orientation (*6*). In the present study, we found that *G. oto* serves
371 as an excellent model to study differences in bristle and scale morphogenesis, as the wing
372 contains a wide range of different scale types. In the developing bristle-like scales, we find
373 symmetrical actin bundles that outline the cell periphery and a large population of
374 longitudinally running interior microtubules. This is similar to what has been described for
375 developing bristles in *Drosophila melanogaster* pupae, which contain peripheral bundles
376 of cross-linked actin filaments and a large population of microtubules that run
377 longitudinally along the bristle (*30*). Recently, (*31*) showed that actin bundles play
378 different roles in shaping scales and bristles in the mosquito *Aedes aegypti*, in which
379 developing bristles contained symmetrically organized actin bundles, while actin bundle
380 distribution in scales became more asymmetrically organized. Given that actin dynamics
381 play a variety of roles in regulating the development of bristles and scales (*6, 7, 31, 32*),
382 we hypothesize that modifications in F-actin organization of scales in the transparent wing
383 of *G. oto* are responsible in part for their narrow bristle-like and forked morphologies. In
384 *D. melanogaster*, subunits of actin are rapidly added to the barbed ends of the actin
385 filaments of bristles, relying on actin polymerization and bundling for this purpose, and
386 cross-linking proteins are required early to bring filaments together (*30*). One cross-
387 linking protein, Fascin, connects filaments together into hexagonally packed bundles. Our

388 TEM of actin bundles, along with previous studies, support a similar mechanism of
389 hexagonally packed F-actin bundles in Lepidoptera (Fig. 3, fig. S1) (*6, 7*).

390 In animal cells, microtubules have been frequently observed in arrangements
391 parallel to the long axis of cellular extensions, such as axons, dendrites, and developing
392 lepidopteran scales (*32*). In an analysis of moth scale development, major shape changes
393 were found to be correlated with changes to the orientation of the cytoplasmic
394 microtubules (*32*). In the present study, we identified large populations of microtubules
395 organized throughout developing scales and showed that microtubules are more
396 concentrated at the base of the scale. We also found that microtubules exhibit different
397 distributions and orientations relative to distinct scale morphologies, namely between
398 bristle, forked, and flat, round scales. In *D. melanogaster*, it has been suggested that bristle
399 microtubules play a role in elongation, noting that they are highly stable, form at the start
400 of the elongation, and then extend along the shaft as the cell elongates (*30*). A more recent
401 reinvestigation of the role of MTs in *D. melanogaster* bristle elongation suggests that two
402 populations of microtubules help to guide bristle development: dynamic microtubules
403 (with mixed polarity) add bulk to the bristle cytoplasm and are thought to contribute
404 proper axial growth, while stable microtubules act to polarize the axis of bristle elongation
405 and are believed to aid organelle and protein distribution (*33, 34*). It would be interesting
406 for future studies to functionally characterize the role microtubules play in the
407 development of lepidopteran scales. Overall, we found conservation of developmental
408 processes in scale formation relative to other previously described Lepidoptera, with
409 notable differences in clear versus opaque wing regions. These findings lend further
410 support that general patterns of scale development, including patterns of F-actin
411 localization and microtubule distribution, seem to be well conserved in Lepidoptera, and
412 that modifications of scale morphology to achieve clearwing phenotypes, such as narrow

413 bristle-like and forked scales, likely involve alteration of cytoskeletal organization during
414 scale growth.

415 Chitinous wing membrane has a higher refractive index than air, so as a
416 mechanism that reduces glare, some clearwing species have evolved sub-wavelength anti-
417 reflective nanostructures (*9, 10*). In this study, we identified the early developmental
418 processes of nanostructures that arise in the wing epithelium. We also note interesting
419 parallels of our observations to previous descriptions of developing nanostructures on the
420 surface of insect cornea. Early data on pupal development of corneal nanostructures were
421 produced by detailed electron microscopy studies, showing that corneal nipples emerge
422 during lens formation, and a chitinous layer may be subsequently secreted underlying
423 the nanostructure (*35*). In these observations, development of initial laminar patches
424 formed on top of underlying microvilli. Subsequently, nanostructures (termed nipple
425 structure array) formed on the surface, with the tips of microvilli still attached to the inner
426 surface. Another study subsequently investigated pupal eye development in *D.*
427 *melanogaster* and identified features of corneal nipple array formation that matched
428 observations previously made in moth eye nanostructure development (*36*). Gemne (*35*)
429 proposed that the corneal nanostructures originate from secretion by the regularly spaced
430 microvilli of the cone lens cells, although there is still debate about the exact nature of
431 how microvilli pre-pattern nanostructure arrays (*37*). Our TEM results provide insight
432 into the early developmental processes of anti-reflective nanostructure formation in the
433 wings of *G. oto,* highlighting certain similarities to nipple array development in insect
434 cornea. It would be interesting for future work to explore if features of nanostructure
435 formation arose independently in insect cuticle as a mechanism to reduce surface
436 reflection.

437 In contrast to previously described highly ordered nipple arrays on insect eyes (e.g.
438 *18, 37*), the irregularly sized anti-reflective nanopillars in the clear regions of *G. oto* wings
439 consist of an upper layer of wax-based epicuticle sitting above procuticle-based nipple
440 nanostructures. Insect cuticle is an extracellular matrix formed by the epidermis and
441 composed of three layers: the outermost envelope, the middle epicuticle and the inner
442 procuticle (*38*). The envelope and the epicuticle are composed mainly of lipids and
443 proteins, while the procuticle contains the polysaccharide chitin. Many terrestrial
444 arthropods deposit a layer of wax lipids on the surface of their cuticle, which reduces
445 evaporative water loss (*39*). In some species of dragonfly, epicuticular wax-based
446 nanostructures have also been demonstrated to play a role in generating optical properties,
447 such as an ultraviolet reflection (*26*). In this study, a dense wax secretion composed of
448 long-chain methyl ketones, in particular 2-pentacosanone, was found to contribute to the
449 UV reflection properties. A recent study also investigated the chemical composition of
450 nanopillars on the wing surface of cicadas, which have been shown to contribute to
451 wettability and antimicrobial properties, and found that the major epicuticular components
452 were fatty acids and hydrocarbons ranging from C_{17} to C_{44} (*40*). Another study exploring
453 the molecular organization of dragonfly wing epicuticle found that the major components
454 identified were fatty acids and *n*-alkanes with even numbered carbon chains ranging from
455 C_{14} to C_{30} (*41*). In the present study, we identified that the epicuticular layer of irregularly
456 sized anti-reflective nanopillars in *G. oto* appear to be composed mainly of *n*-alkanes,
457 including pentacosane (C_{25}) and heptacosane (C_{27}) and showed the importance of these
458 structures to attain better transparency.

459 Due to thin film optics, the thin membranes of insect wings sometimes reflect
460 distinct structural coloration and iridescence (*42*). However, variability and non-constant
461 thickness can make the wing membranes act as non-ideal thin films, and additional surface

462 nanoprotrusions can introduce a gradient of refractive indices that reduces thin film
463 reflections (*43*). For instance, membrane thickness was found to vary over the transparent
464 wings of the damselfy *Hetaerina americana* from below 1 μm to up to 3 μm, yet
465 membrane nanoprotrusions acted as an effective impedance matching device to reduce
466 reflectance (*43*). In that study, average reflectance spectra for the Andromica clearwing
467 butterfly *Greta andromica* was also calculated, although the wing was treated as a thin
468 film, and did not take into account membrane surface nanostructures. By varying
469 thickness in a Gaussian way while maintaining average thickness, (*43*) found that an
470 increasing width of the Gaussian progressively reduced modulation of the reflectance
471 spectrum. Similarly, in the present study, measurements from SEM cross sections of *G.*
472 *oto* transparent wings indicate that the membrane thickness is non-constant, and in our
473 optical simulations, variance in membrane thickness was found to be an important
474 parameter for reduced reflectance spectra modulation (fig. S3). Overall, we found that
475 variance in membrane thickness and wax-based nanostructures with irregular height
476 distributions in *G. oto* reduce iridescence and maintain anti-reflection properties, which
477 likely aid in crypsis to reduce predation (*11*).

478 Turing reaction-diffusion mechanisms have been proposed as a model for the
479 formation of various corneal nanostructure morphologies (such as spacing, height, and
480 spatial organization) during insect eye development (reviewed in *37*). Although the degree
481 of height irregularity of nanopillars is important for achieving omnidirectional anti-
482 reflection in *G. oto*, we do not yet understand how the wax nanopillars are generated to
483 vary in height. Perhaps the pressure of the wax secretion varies across the microvillar
484 extensions' area, similar to how nozzle area plays a role in the propulsion force, and tunes
485 the height of the nanopillars in the process. In such a scenario, the degree of the height
486 variation could be synthetically engineered depending on the two-dimensional

487 nanopatterned mask design in the biomimetic processes, like molding or imprinting
488 techniques. Additionally, previous studies have generated three-dimensional wax
489 structures by using *n*-alkanes, noting that wax-based crystals can generate different
490 shapes, sizes and densities depending on the chain length (*44*). Future work should
491 investigate the possible role of alkanes, and the two-dimensional surface growth geometry,
492 in generating three-dimensional anti-reflective nanostructures and potential applications
493 for biomimetics. Additionally, the present study exploring *Greta oto* wing development
494 can serve as a basis for understanding how transparent phenotypes evolved within
495 Ithomiini, a diverse tribe of neotropical butterflies that act as mimicry models for
496 numerous species of Lepidoptera (*25*), as well as more distantly related butterfly and moth
497 species.

498

499 **Materials and Methods**

500 **Samples**

501 Glasswing butterfly (*Greta oto*) pre-pupae were purchased from Magic Wings Butterfly
502 House (Deerfield, Massachusetts, USA) and reared on *Cestrum nocturnum* leaves at 27°C
503 and 60% humidity on a 16:8 hour light:dark cycle at the Marine Biological Laboratory
504 (Woods Hole, MA) under the United States Department of Agriculture permit number
505 P526P-19-02269. At the appropriate time of development, pupal wings were dissected and
506 age was recorded as hours after pupal case formation (h APF) as in (*6*). The average
507 timeline from pupation to eclosion (adult emergence) for *G. oto* at 27°C is about 7 days,
508 and we report our time series here which covers early aspects of wing scale development.

509

510 **Optical imaging and scale measurements**

511 Images of whole mounted specimens were taken with a Canon EOS 70D digital camera
512 with an EF 100mm f/2.8L macro lens. High-magnification images of disarticulated wings
513 were taken with a Keyence VHX-5000 digital microscope. Scale density was determined
514 by counting the numbers of scales in a 1 mm^2 area. Scales were also removed from the
515 wings, laid flat onto a slide, and Keyence software was used to measure the surface area of
516 individual scales. Images of clear and opaque regions were processed with Keyence
517 software to measure the percentage of area covered by scales. Sample size was equal to
518 three individual butterflies reared in the same cohort, in which four measurements for each
519 individual were averaged. We performed Student's t-tests for scale density and percent of
520 exposed membrane, and one-way ANOVA test for scale surface area comparisons.

521

522 **Confocal microscopy**

523 For confocal microscopy of fixed tissue, pupal wings were dissected and fixed in PIPES,
524 EGTA, $MgSO_4$ (PEM) buffer with 3.7% paraformaldehyde for 20-30 minutes at room
525 temperature, as described previously (*6*). Fixed wings were incubated in 1X PBS+0.1%
526 Triton-X 100 (PT) with 1:200 dilution of phalloidin, Alexa 555 conjugated (Invitrogen
527 A34055), and Wheat Germ Agglutinin, Alexa 647 conjugated (Invitrogen W32466) at a
528 dilution of 1:200 overnight at 4°C. Wings were washed in PT and then placed in 50%
529 glycerol:PBS with 1 μg/mL DAPI overnight at 4°C. Wing samples were placed on
530 microscope slides and mounted in 70% glycerol:PBS. A coverslip (#1.5 thickness) was
531 applied, and each preparation was sealed with nail polish. Slides of fixed tissue were
532 examined with an LSM 880 confocal microscope (Carl Zeiss, Germany) with 40x and 63x
533 objectives. Confocal images and movies were generated using Imaris Image Analysis
534 Software (Bitplane, Oxford Instruments, UK).

535

536 **Scanning electron microscopy**

537 We cut 2mm square pieces from dry wings, coated them with a 10 nm layer of gold using
538 the BIO-RAD E5400 Sputter Coater, and imaged with a Hitachi TM-1000 SEM at 5 kV.
539 Top-view and cross section SEM images were analysed with ImageJ 1.52 to measure
540 membrane thickness and nanostructure dimensions (n = 6).

541

542 **Transmission electron microscopy**

543 For transmission electron microscopy, wings of *Greta oto* pupae were dissected and fixed
544 in 2% glutaraldehyde, 2% paraformaldehyde in 0.1 M sodium cacodylate buffer overnight
545 at 4°C (pH 7.4). Samples were then rinsed in 0.1 M cacodylate buffer (pH 7.4) and post-
546 fixed in1% aqueous osmium tetroxide in 0.1M cacodylic buffer overnight at 4°C, then
547 rinsed in water. Samples were en bloc stained with 1% uranyl acetate in water and then
548 rinsed in water. Samples were dehydrated through a graded ethanol series (50–100% in
549 10% steps), rinsed in propylene oxide, then infiltrated in 50% resin and propylene oxide
550 overnight. Samples were infiltrated with Epon/Alardite embedding medium (70%, 80%,
551 95% to 100% steps) and polymerized at 60°C for two days. Thin sections (~70nm) were
552 cut on an Ultramicrotome RMC PowerTome XL using a Diatome diamond knife. Digital
553 images were taken using a JEOL 200 transmission electron microscope (Jeol, USA).

554

555 **Wing surface wax extraction and analysis**

556 To identify the molecular composition of the transparent wing surface, we pooled wing
557 dissections from three individual adults and performed two replicates for chloroform-
558 based extractions and two replicates for hexane-based extractions (after *26*). First, the
559 samples were soaked with 100 μL of either hexane or chloroform and gently mixed for 15

560 minutes on a Thermolyne RotoMix 51300. The liquid solutions containing dissolved wing
561 surface compounds were then transferred to glass vials with fixed microvolume inserts
562 and the solvent was evaporated under a stream of high-purity nitrogen gas (99.99%).
563 Dried extracts were re-dissolved in fixed volumes of hexane (10 μL), and half of the
564 extract (5 µl) was injected by automatic liquid sampler into a gas chromatograph coupled
565 with a mass selective detector (GC: 7890A; MS: 5975C; Agilent Technologies, USA)
566 operating in electron impact mode. The injection was performed in a split/splitless injector
567 in the splitless mode. Separation of compounds was performed on a fused silica capillary
568 column (DB-5MS, 30 m × 0.32 mm × 0.25 µm, Agilent J&W GC columns, USA) with a
569 temperature program starting from 80°C for 5 min and increasing by 80°C per min to 200
570 °C, followed by an increase of 5 °C per min to 325 °C which was held for 3 min, with
571 helium used as the carrier gas, positive electron ionization (70 eV), Analog to Digital
572 (A/D) sampling rate was set at 4, and the scan range was m/z 40.0 to 650.0. Chemical data
573 processing was carried out using the software "Enhanced Chemstation" (Agilent
574 Technologies, USA). We retained peaks with abundances greater than 0.25% of the total
575 and compounds were identified according to their retention indices, diagnostic ions, and
576 mass spectra, which are provided in Table S1. For some peaks, it was not possible to
577 narrow the identity to a single specific compound because (1) some low abundance
578 substances produced poor quality mass spectra, (2) multiple compounds could have
579 produced the observed fragmentation patterns and/or (3) multiple compounds may have
580 co-eluted at the same retention time.
581

582 **Optical measurements**

583 The wing reflection measurements were performed on a Cary 5000 UV-Vis-NIR
584 spectrophotometer, equipped with a light source of tungsten halogen and an integrating

585 sphere diffuse reflectance accessory (Internal DRA 1800). Wing measurements from the
586 dorsal wing surface (n = 6) were recorded with unpolarized light with a spot size of 100
587 μm for an incident angle of 8° to avoid the loss of direct specular reflectance component
588 through the aperture. All measurements were taken in the dark to avoid possible stray
589 illumination from the surrounding environment. A reference measurement was done with
590 a calibrated commercial white spectralon standard to calculate the relative diffuse
591 reflectance. The reflectance measurements and mean data are presented in Table S2.
592

593 **Optical simulations**

594 The reflectance of the wing membrane before and after chemical treatment by hexane was
595 analytically modeled using effective medium theory and transfer matrix method (*10, 18*).
596 First, the effective volume fraction of the nanoprotuberances before and after the chemical
597 treatment were based on measurements taken from SEM micrographs of the wings. We used
598 the average distance between two hexagonally arranged nanostructures, d, conical shaped
599 nipple nanostructures with height, h_p, wax-based irregular nanopillars with radius, r_{np}, mean
600 height, h_{np} and variance σ_{np}, and membrane thickness, h_m and variance σ_m (fig. S2). We
601 considered a Gaussian distribution of irregular nanopillar height, as described previously
602 (*10*). We also modeled the membrane thickness with Gaussian distribution to replicate the
603 experimental membrane modulation in the calculation (*43, 45*). The total volume fraction
604 of the untreated wing along the height h can be given by:
605

$$f_{untreated}(h) = \begin{cases} \frac{\pi r_{np}^2}{\sqrt{3}d^2}\mathrm{erfc}\left(\frac{h-h_{np}}{\sigma_{np}\sqrt{2}}\right); & \text{zone: dorsal wax based nanopillar} \\ \frac{\pi}{\sqrt{3}d^2}\left(r_{np} + \left(\frac{d}{2} - r_{np}\right)\left(1 - \frac{h}{h_p}\right)\right)^2; & \text{zone: dorsal chitin-based nipple array} \\ 1; & \text{zone: chitin membrane} \end{cases}$$

$$\frac{\pi}{\sqrt{3}d^2}\left(r_{np}+(\frac{d}{2}-r_{np})\left(1-\frac{h}{h_p}\right)\right)^2;$$ zone: ventral chitin-based nipple array

$$\frac{\pi {r_{np}}^2}{\sqrt{3}d^2}\mathrm{erfc}(\frac{h-h_{np}}{\sigma_{np}\sqrt{2}});$$ zone: ventral wax based nanopillar

where, $\mathrm{erfc(x)} = \frac{2}{\sqrt{\pi}}\int_x^\infty e^{-t^2}dt$ is the complementary error function.

The volume fraction of the treated wing without the irregular nanopillars will be:

$$\underline{f_{treated}(h)} = \begin{cases} \frac{\pi}{2\sqrt{3}}\left(1-\frac{h}{h_p}\right); & \text{zone: dorsal chitin-based nipple array} \\ 1; & \text{zone: chitin membrane} \\ \frac{\pi}{2\sqrt{3}}\left(1-\frac{h}{h_p}\right); & \text{zone: ventral chitin-based nipple array} \end{cases}$$

After determining the volume fraction, the corresponding refractive index changes along the wing at any height *h* was calculated using the effective medium theory with the Maxwell-Garnett approximation as shown in Fig. 6E, fig. S2. The refractive indices of the different materials were considered as $n_{air} = 1$, $n_{chitin} = 1.56 + i0.008$ (*20, 21*) and we considered $n_{wax} = 1.39$ (based on *46*). Afterwards, the transfer matrix method computed the reflectance from the stratified medium with calculated refractive index profiles as shown in Fig. 6E for the unpolarized condition (taking the average of both s- and p-polarization) at an incident angle of 8°. The membrane-only reflection at normal incident light can be directly calculated from (*45*):

$$R\ (\lambda) = \int_0^\infty \left|\frac{r(1-e^{-2i\delta})}{1-r^2e^{-2i\delta}}\right|^2 \frac{1}{\sigma_m\sqrt{2\pi}} e^{\frac{-(h-h_m)^2}{2\sigma_m^2}}\ dh.$$

Where, $\delta = (2\pi n_{chitin}h)/\lambda$ is the phase delay introduced by the membrane thickness of *h*, and *r* is the reflection coefficient at the air-chitin boundary governed by Fresnel's equation for a normal incident light, i.e., $r = (1 - n_{chitin}) / (1 + n_{chitin})$.

522 **References and Notes**

523 1. P. Beldade, P. M. Brakefield. The genetics and evo–devo of butterfly wing patterns.
524 *Nature Reviews Genetics*. **3**, 442-52 (2002).
525 2. R. O. Prum, T. Quinn, R. H. Torres. Anatomically diverse butterfly scales all produce
526 structural colours by coherent scattering. *Journal of Experimental Biology*. **209**, 748-
527 65. (2006).
528 3. L. E. Gilbert, M. C. Singer. Butterfly ecology. *Ann. Rev. Ecol. Syst*. **6**, 365-95 (1975).
529 4. D. G. Stavenga, H. L. Leertouwer, B. D. Wilts. Coloration principles of nymphaline
530 butterflies–thin films, melanin, ommochromes and wing scale stacking. *J. Exper. Biol*.
531 **217**, 2171-80 (2014).
532 5. R. C. Thayer, F. I. Allen, N. H. Patel. Structural color in *Junonia* butterflies evolves by
533 tuning scale lamina thickness. *Elife*. **9**, e52187 (2020).
534 6. A. Dinwiddie, R. Null, M. Pizzano, L. Chuong, A. L. Krup, H. E. Tan, N. H. Patel.
535 Dynamics of F-actin prefigure the structure of butterfly wing scales. *Develop. biol*.
536 **392**, 404-18 (2014).
537 7. A. R. Day, J. J. Hanly, A. Ren, A. Martin. Sub-micrometer insights into the
538 cytoskeletal dynamics and ultrastructural diversity of butterfly wing scales.
539 *Developmental Dynamics*. **248**, 657-70 (2019).
540 8. P. P. Goodwyn, Y. Maezono, N. Hosoda, K. Fujisaki. Waterproof and translucent
541 wings at the same time: problems and solutions in butterflies. *Naturwissenschaften*.
542 **96**, 781-7 (2009).
543 9. A. Yoshida, M. Motoyama, A. Kosaku, K. Miyamoto. Antireflective
544 nanoprotuberance array in the transparent wing of a hawkmoth, *Cephonodes hylas*.
545 *Zoological sci*. **14**, 737-41 (1997).
546 10. R. H. Siddique, G. Gomard, H. Hölscher. The role of random nanostructures for the
547 omnidirectional anti-reflection properties of the glasswing butterfly. *Nature*
548 *communications*. 6, 1-8 (2015).
549 11. M. Arias, J. Mappes, C. Desbois, S. Gordon, M. McClure, M. Elias, O. Nokelainen, D.
550 Gomez. Transparency reduces predator detection in mimetic clearwing butterflies.
551 *Func. Ecol*. **33**, 1110-9 (2019).
552 12. M. Arias, M. Elias, C. Andraud, S. Berthier, D. Gomez. Transparency improves
553 concealment in cryptically coloured moths. *J. Evol. Biol*. **33**, 247-52 (2020).

13. M. Mcclure, C. Clerc, C. Desbois, A. Meichanetzoglou, M. Cau, L. Bastin-Héline, J. Bacigalupo, C. Houssin, C. Pinna, B. Nay, V. Llaurens. Why has transparency evolved in aposematic butterflies? Insights from the largest radiation of aposematic butterflies, the Ithomiini. *Proc. Royal Soc. B*. **286**, 20182769 (2019).
14. S. Johnsen. Hidden in plain sight: the ecology and physiology of organismal transparency. *The Biological Bulletin*. **201**, 301-18 (2001).
15. S. Johnsen. Hide and seek in the open sea: pelagic camouflage and visual countermeasures. *Annual review of marine science*. **6**, 369-92 (2014).
16. L. E. Bagge. Not as clear as it may appear: challenges associated with transparent camouflage in the ocean. *Integ. compar. biol*. **59**,1653-63 (2019).
17. C. G. Bernhard, W. H. Miller. A corneal nipple pattern in insect compound eyes. *Acta Physiologica Scandinavica*. **56**, 385-6 (1962).
18. D. G. Stavenga, S. Foletti, G. Palasantzas, K. Arikawa. Light on the moth-eye corneal nipple array of butterflies. *Proc. Royal Soc. B: Biological Sciences*. **273**, 661-7 (2006).
19. Y. F. Huang, Y. J. Jen, L. C. Chen, K. H. Chen, S. Chattopadhyay. Design for approaching cicada-wing reflectance in low-and high-index biomimetic nanostructures. *ACS nano*. **9**, 301-11 (2015).
20. P. Vukusic, J. R. Sambles, C. R. Lawrence, R. J. Wootton. Quantified interference and diffraction in single Morpho butterfly scales. *Proc. Royal Soc. London. Series B: Biol. Sci*. **266**, 1403-11 (1999).
21. V. Narasimhan, R. H. Siddique, J. O. Lee, S. Kumar, B. Ndjamen, J. Du, N. Hong, D. Sretavan, H. Choo. Multifunctional biophotonic nanostructures inspired by the longtail glasswing butterfly for medical devices. *Nature nanotechnology*. **13**, 512-9 (2018).
22. O. Deparis, S. R. Mouchet, L. Dellieu, J. F. Colomer, M. Sarrazin. Nanostructured surfaces: bioinspiration for transparency, coloration and wettability. *Mater. Today Proc. S*. **1**, 122-9 (2014).
23. V. R. Binetti, J. D. Schiffman, O. D. Leaffer, J. E. Spanier, C. L. Schauer. The natural transparency and piezoelectric response of the *Greta oto* butterfly wing. *Integr. Biol*. **1**, 324-9 (2009).
24. D. Gomez, C. Pinna, J. Pairraire, M. Arias, J. Barbut, A. Pomerantz, C. Nous, W. D. de Marcillac, S. Berthier, N. Patel, C. Andraud, M. Elias. Transparency in butterflies and moths: structural diversity, optical properties and ecological relevance. *bioRxiv*. doi: https://doi.org/10.1101/2020.05.14.093450 (2020).

587 25. M. Elias, Z. Gompert, C. Jiggins, K. Willmott. Mutualistic interactions drive
588 ecological niche convergence in a diverse butterfly community. *PLoS biology*. **6**, e300
589 (2008).
590 26. R. Futahashi, Y. Yamahama, M. Kawaguchi, N. Mori, D. Ishii, G. Okude, Y. Hirai, R.
591 Kawahara-Miki, K. Yoshitake, S. Yajima, T. Hariyama. Molecular basis of wax-based
592 color change and UV reflection in dragonflies. *Elife*. **8**, e43045 (2019).
593 27. H. T. Ghiradella, M. W. Butler. Many variations on a few themes: a broader look at
594 development of iridescent scales (and feathers). *J. Royal Soc. Interface*. Apr **6**, S243-
595 51 (2009).
596 28. R. D. Reed. Evidence for Notch-mediated lateral inhibition in organizing butterfly
597 wing scales. *Development Genes and Evolution*. **214**, 43-6 (2004).
598 29. R. Galant, J. B. Skeath, S. Paddock, D. L. Lewis, S. B. Carroll. Expression pattern of a
599 butterfly achaete-scute homolog reveals the homology of butterfly wing scales and
700 insect sensory bristles. *Current Biology*. **8**, 807-13 (1998).
701 30. I. G. Tilney, P. S. Connelly, K. A. Vranich, M. K. Shaw, G. M. Guild. Actin filaments
702 and microtubules play different roles during bristle elongation in *Drosophila*. *J. Cell.*
703 *Sci*. **113**, 1255-65 (2000).
704 31. S. Djokic, B. Anna, I. Zurim, N. Urakova, J. Ragson, U. Abdu. Actin bundles play
705 different role in shaping scale as compare to bristle in mosquito *Aedes aegypti*.
706 *bioRxiv*. doi: https://doi.org/10.1101/2020.04.06.027110 (2020).
707 32. I. Overton. Microtubules and microfibrils in morphogenesis of the scale cells of
708 *Ephestia kuhniella*. *J. cell biology*. **29**, 293-305 (1966).
709 33. A. Bitan, G. M. Guild, D. Bar-Dubin, U. Abdu. Asymmetric microtubule function is
710 an essential requirement for polarized organization of the Drosophila bristle. *Molec.*
711 *cell. biol*. **30**, 496-507 (2010).
712 34. A. Bitan, I. Rosenbaum, U. Abdu. Stable and dynamic microtubules coordinately
713 determine and maintain *Drosophila* bristle shape. *Development*. **139**, 1987-96 (2012).
714 35. G. Gemne. Ontogenesis of corneal surface ultrastructure in nocturnal Lepidoptera.
715 *Philosophical Transactions of the Royal Society of London. B, Biological Sciences*.
716 **262**, 343-63 (1971).
717 36. A. Fröhlich. A scanning electron-microscopic study of apical contacts in the eye
718 during postembryonic development of *Drosophila melanogaster*. *Cell and tissue*
719 *research*. **303**, 117-28 (2001).

37. M. Kryuchkov, A. Blagodatski, V. Cherepanov, V. L. Katanaev. "Arthropod corneal nanocoatings: diversity, mechanisms, and functions" in Functional Surfaces in Biology III. (Springer, Cham, Switzerland, 2017), pp. 29-52.
38. B. Moussian. Recent advances in understanding mechanisms of insect cuticle differentiation. *Insect biochem. molec. biol.* **40**, 363-75 (2010).
39. A. G. Gibbs. Water-proofing properties of cuticular lipids. American Zoologist. **38**, 471-82 (1998).
40. I. Román-Kustas, J. B. Hoffman, J. H. Reed, A. E. Gonsalves, J. Oh, L. Li, S. Hong, K. D. Jo, C. E. Dana, N. Miljkovic, D. M. Cropek. Molecular and Topographical Organization: Influence on Cicada Wing Wettability and Bactericidal Properties. *Advanced Materials Interfaces*. **7**, 2000112 (2020).
41. A. P. Ivanova, S. H. Nguyen, H. K. Webb, J. Hasan, V. K. Truong, R. N. Lamb, X. Duan, M. J. Tobin, P. J. Mahon, R. J. Crawford. Molecular organization of the nanoscale surface structures of the dragonfly *Hemianax papuensis* wing epicuticle. *PLoS One*. **8**, e67893. (2013).
42. A. Shevtsova, C. Hansson, D. H. Janzen, J. Kjærandsen. Stable structural color patterns displayed on transparent insect wings. *Proc. Natl. Acad. Sci.* **108**, 668-73 (2011).
43. D. G. Stavenga. Thin film and multilayer optics cause structural colors of many insects and birds. *Materials Today: Proceedings*. **1**, 109-21 (2014).
44. A. Gorb, S. Böhm, N. Jacky, L. P. Maier, K. Dening, S. Pechook, B. Pokroy, S. Gorb. Insect attachment on crystalline bioinspired wax surfaces formed by alkanes of varying chain lengths. *Beilstein J. Nanotech*. **5**, 1031-41 (2014).
45. R. H. Siddique, S. Vignolini, C. Bartels, I. Wacker, H. Hölscher. Colour formation on the wings of the butterfly *Hypolimnas salmacis* by scale stacking. *Scientific reports*. **6**, 36204 (2016).
46. I. R. Hooper, P. Vukusic, R. J. Wootton. Detailed optical study of the transparent wing membranes of the dragonfly *Aeshna cyanea*. *Optics express*. **14**, 4891-7 (2006).

Acknowledgments

We would like to thank the Angie Serrano, Paola Betucci, Idoia Quintana-Urzainqui and Helena Bilandzija from the MBL Embryology Course and Cao Lu Yan from the MBL Physiology Course for their preliminary work on scale morphology of clearwing Lepidoptera, and subsequent work by Jaap van Krugten, Raymundo Picos, and Johnny On at UC Berkeley. We also thank Rachel Thayer, Arnaud Martin, Damien Gailly, Melanie Mcclure, Luca Livraghi, Oscar Paneso, Rémi Mauxion and Owen McMillan for their assistance with fieldwork, rearing, and preliminary experiments. We thank Fred Gagnon of Magic Wings Butterfly Conservatory and Gardens for assistance with butterfly rearing and Neil Tsutsui for support with the GC-MS experiments. Members of the Patel Lab and Craig Miller provided helpful feedback on the manuscript. RHS acknowledges the support from the Beckman Institute of the California Institute of Technology to the Molecular Materials Research Center. **Funding:** This work was supported by a grant from the Human Frontier Science Program (RGP0014/2016), a France-Berkeley fund grant (FBF #2015--58) and an ANR grant (CLEARWING project, ANR-16-CE02-0012). **Author contributions:** Conceived and designed the experiments: AFP and NHP. Performed the experiments: AFP, RHS, EIC, KH. All authors contributed to analysis of the results, contributed reagents/materials/analysis tools and contributed to writing the paper. **Competing interests:** The authors declare they have no competing interests.

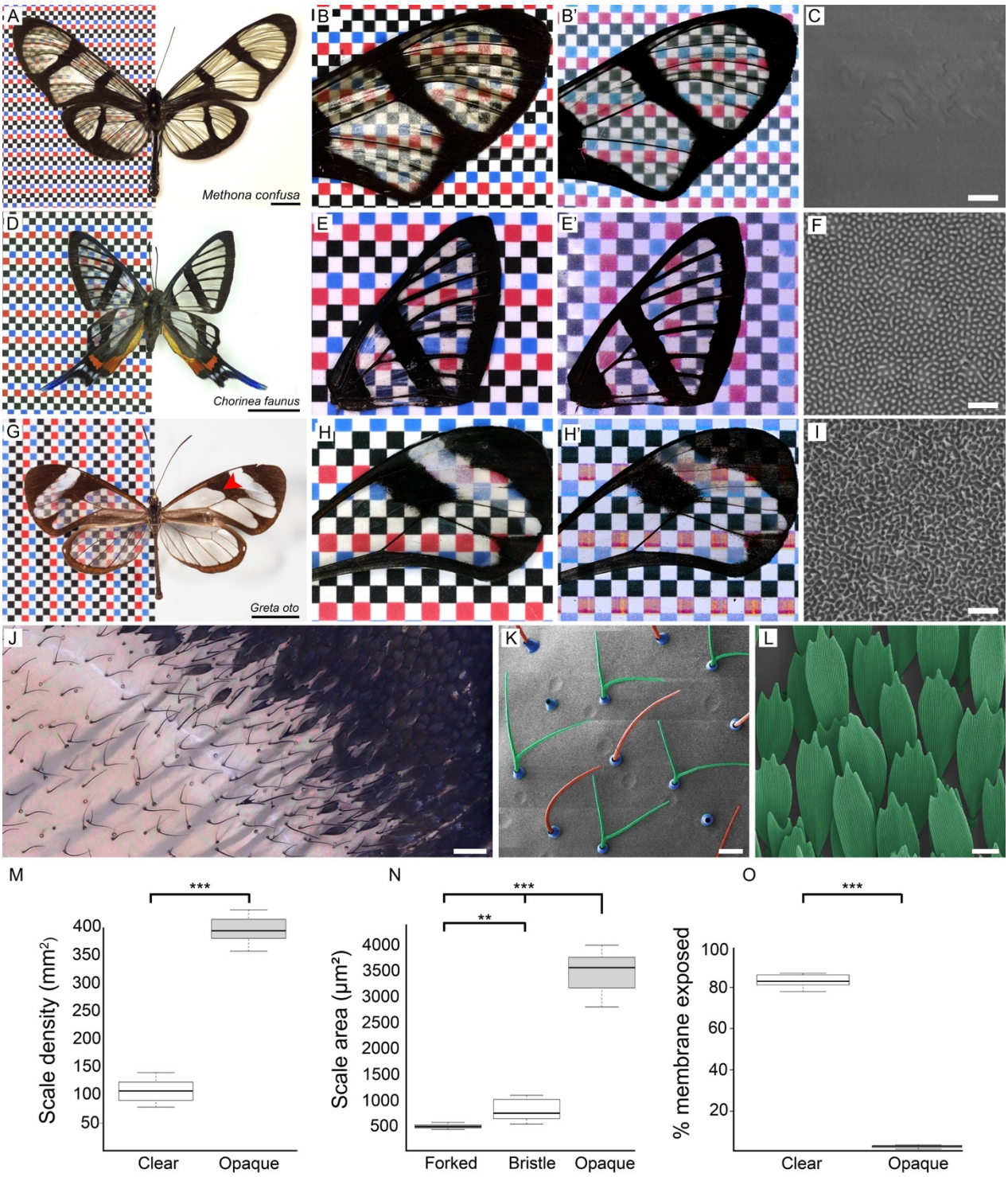

Fig. 1. Examples of clearwing butterflies and wing scale features in *Greta oto*

(A) Giant glasswing *Methona confusa* (Nymphalidae: Ithomiini). Scale bar = 1 cm. Wings under **(B)** reflected and **(B')** transmitted light illustrating general transparency, but strong light reflectance off the wing surface in this species. **(C)**

775 The surface of the wing membrane is smooth and devoid of nanostructures. Scale
776 bar = 1 μm. **(D)** Longtail glasswing *Chorinea faunus* (Riodinidae). Scale bar = 1
777 cm. Wings under **(E)** reflected and **(E')** transmitted light illustrating minimal
778 reflectance. **(F)** The membrane surface contains dome-shaped chitin
779 nanoprotuberances that generate anti-reflective properties (*21*). Scale bar = 1 μm.
780 **(G)** Glasswing *Greta oto* (Nymphalidae: Ithomiini). Red arrowhead indicates the
781 representative clear and opaque wing region investigated, scale bar = 1 cm. Wings
782 under **(H)** reflected and **(H')** transmitted light illustrating minimal reflectance. **(I)**
783 The surface of the wing membrane contains irregularly sized nanopillars that
784 enable omnidirectional anti-reflective properties (*10*). Scale bar = 1 μm. **(J)** High
785 magnification of a transition boundary between a clear (left side) and opaque
786 (upper right side) wing region in *G. oto*. Scale bar = 100 μm. **(K)** SEM of adult
787 scales in a clear wing region of *G. oto*, revealing the alternating forked (green false
788 coloring) and bristle-like (red false coloring) scale morphologies (socket false
789 colored in blue). Scale bar = 20 μm. **(L)** SEM of scales in an opaque wing region
790 in *G. oto*, highlighting typical large, flat scale morphologies. Scale bar = 20 μm.
791 **(M)** Measurements of scale density in clear and opaque wing regions, **(N)** scale
792 surface area for forked, bristle-like, and opaque scale morphologies, and **(O)**
793 percent of wing membrane exposed in *G. oto* clear and opaque regions. Error bars
794 indicate means + SD of four measurements taken from wings in three different
795 individuals, P-values are based on Student's t-test for **(M)**, **(O)**, and ANOVA test
796 for **(N)**, ***$P < 0.001$; **$P < 0.01$.

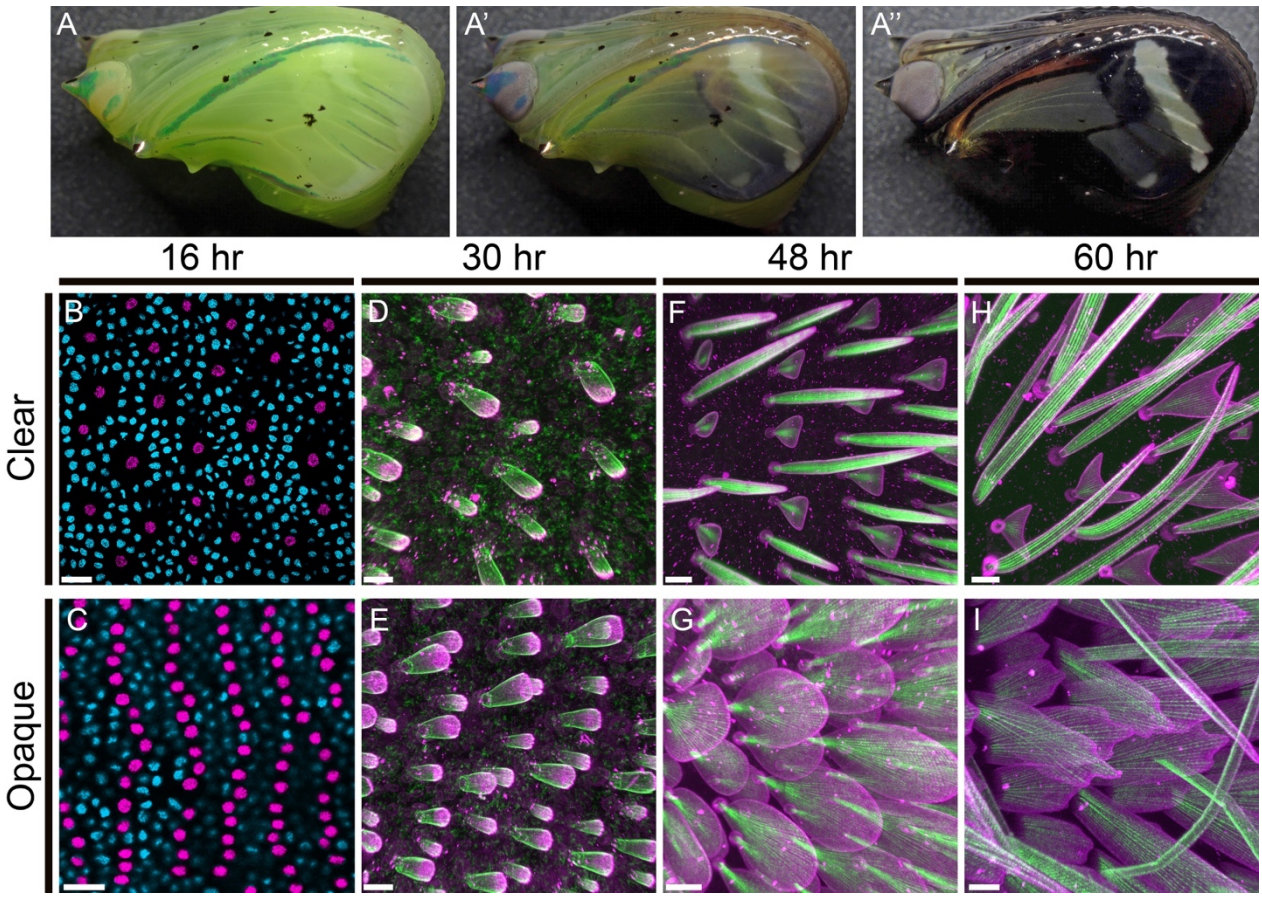

Fig. 2. Pupal wing development and cytoskeletal organization of scales in clear and opaque regions

(A) Representative image of a *Greta oto* pupa ~5 days after pupal formation (APF), **(A'-A'')** developing up to the melanic stage ~7 days APF, just prior to eclosion. **(B)** Early wing development 16 hours APF stained with DAPI (nuclei) in a clear wing region and **(C)** opaque wing region. The clear region contains a reduced number of sensory organ precursor (SOP) cells (which are the precursor cells to the scale and socket cells) relative to the opaque region. Scale bar = 20 μm. SOP cells are false colored magenta for better viewing. Simultaneous confocal imaging of fluorescently labeled scale cell membrane (wheat germ agglutinin; WGA, magenta), and F-actin (phalloidin, green), comparing clear wing regions **(D,**

310 **F, H)** to opaque wing regions **(E, G, I)**. At 30 h AFP **(D, E)** WGA and phalloidin
311 staining reveal early scale buds extending from the wing epithelium. F-actin
312 reveals loosely organized parallel actin filaments protruding from the membrane.
313 48 h APF **(F, G)** scales have grown and changed in morphology. Short actin
314 filaments have reorganized and formed smaller numbers of thick, regularly spaced
315 parallel bundles under the surface of the cell membrane. **(F)** In the clear wing
316 region, scale cells alternate between triangular shapes and bristles. 60 h APF **(H,**
317 **I)**, developing scales have become more elongated. **(H)** The triangular-shaped
318 scales in the clear wing region have proceeded to generate two new branches,
319 which fork and elongate bidirectionally, while bristle-like scales have rapidly
320 elongated and curved. **(I)** In the opaque region, scales are longer, wider, and have
321 now developed serrations at the tips. Scale bar in **(D-I)** = 10 μm.

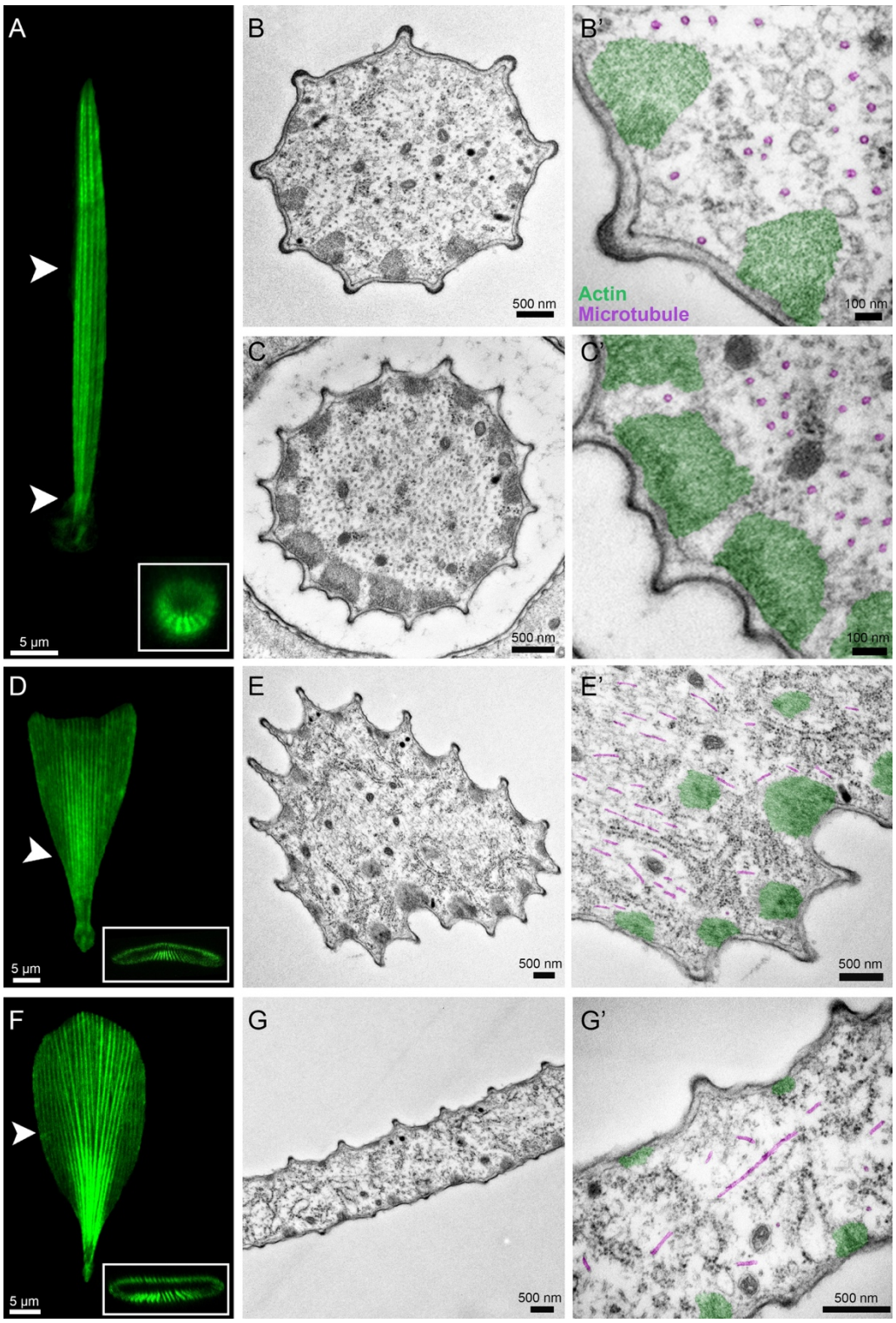

Fig. 3. Confocal and transmission electron microscopy transverse sections of developing bristle (top), forked (middle) and flat (bottom) scales 48 hours APF

825 **(A)** Confocal projection of a bristle-like scale morphology (phalloidin) in a clear
826 wing region. White arrowhead shows representative regions of transverse TEM
827 sections. Scale bar = 5 μm. TEM of a bristle-like scale in a distal region **(B-B')** and
828 a basal region near the socket cell **(C-C')**. Note the peripheral actin bundles (false
829 colored green) and internal microtubule rings (false colored magenta). The more
830 distal region of the scale **(B)** contains a lower density of microtubules relative to
831 the base of the scale **(C)**. Scale bars in **(B,C)** = 500 nm and scale bars in **(B',C')** =
832 100 nm. **(D)** Confocal projection of a developing forked scale (phalloidin) in a
833 clear wing region. White arrowhead shows representative regions of transverse
834 TEM sections. Scale bar = 5 μm. **(E-E')** TEM of a forked scale reveals peripheral
835 bundles of actin (false colored green), with thicker actin bundles on the ventral
836 side of the scale and internal microtubules (false colored magenta). Two internal
837 bundles of actin filaments can be observed in the cytoplasm **(E')**. Scale bars in **(E-**
838 **E')** = 500 nm. **(F)** Confocal projections of developing flat, round scale (phalloidin)
839 in an opaque wing region. White arrowhead shows representative regions of
840 transverse TEM sections. Scale bar = 5 μm. **(G-G')** TEM reveals asymmetry in the
841 actin bundles (false colored green), which are thicker on the bottom side of the
842 scale relative to the upper surface. Microtubules (false colored magenta) are found
843 in various orientations. Scale bar in **(G-G')** = 500 nm.

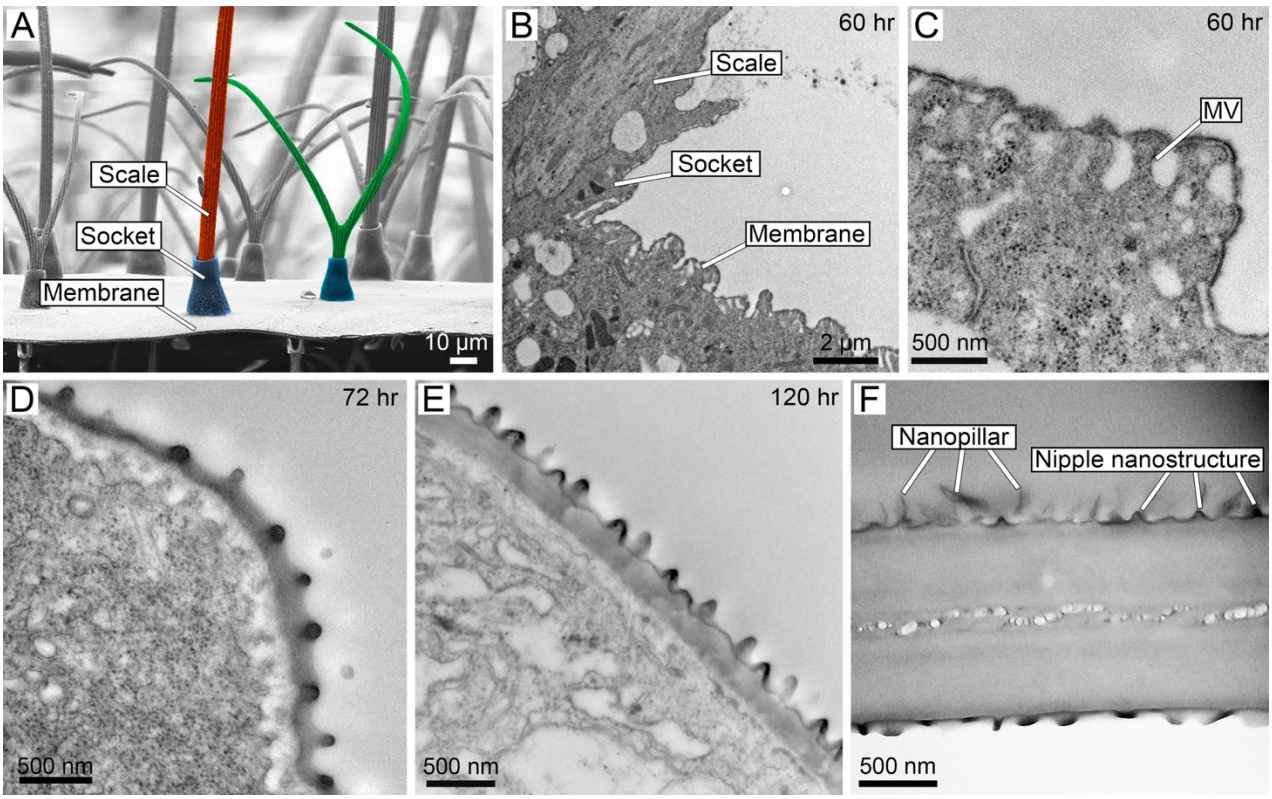

Fig. 4. Ontogeny of wing membrane surface nanostructures

(A) SEM cross section (side view) of an adult *Greta oto* clear wing region. Scale bar = 10 µm. Bristle-like scale false colored in red, forked scale false colored in green, sockets false colered in blue. **(B)** TEM transverse section of epithelial tissue 60 h APF, showing lateral scale growth and wing membrane cells. Scale bar = 2 µm. **(C)** Higher magnification of developing wing epithelial cells at 60 h APF show microvilli (MV) projections, which appear as slender linear extensions from the inner margins of the developing cells that insert into a thin layer of electron-dense material. Lamina evaginations appear in the section as domes. **(D)** TEM of epithelial tissue 72 h APF and **(E)** 120 h APF shows wing surface nanostructures protruding from the surface, with tips of microvilli still attached to the inner surface of the wing membrane. **(F)** TEM of the adult wing membrane. The surface contains dome-shaped nipple nanostructures and an upper layer of nanopillars. Scale bar in **(C-E)** = 500 nm.

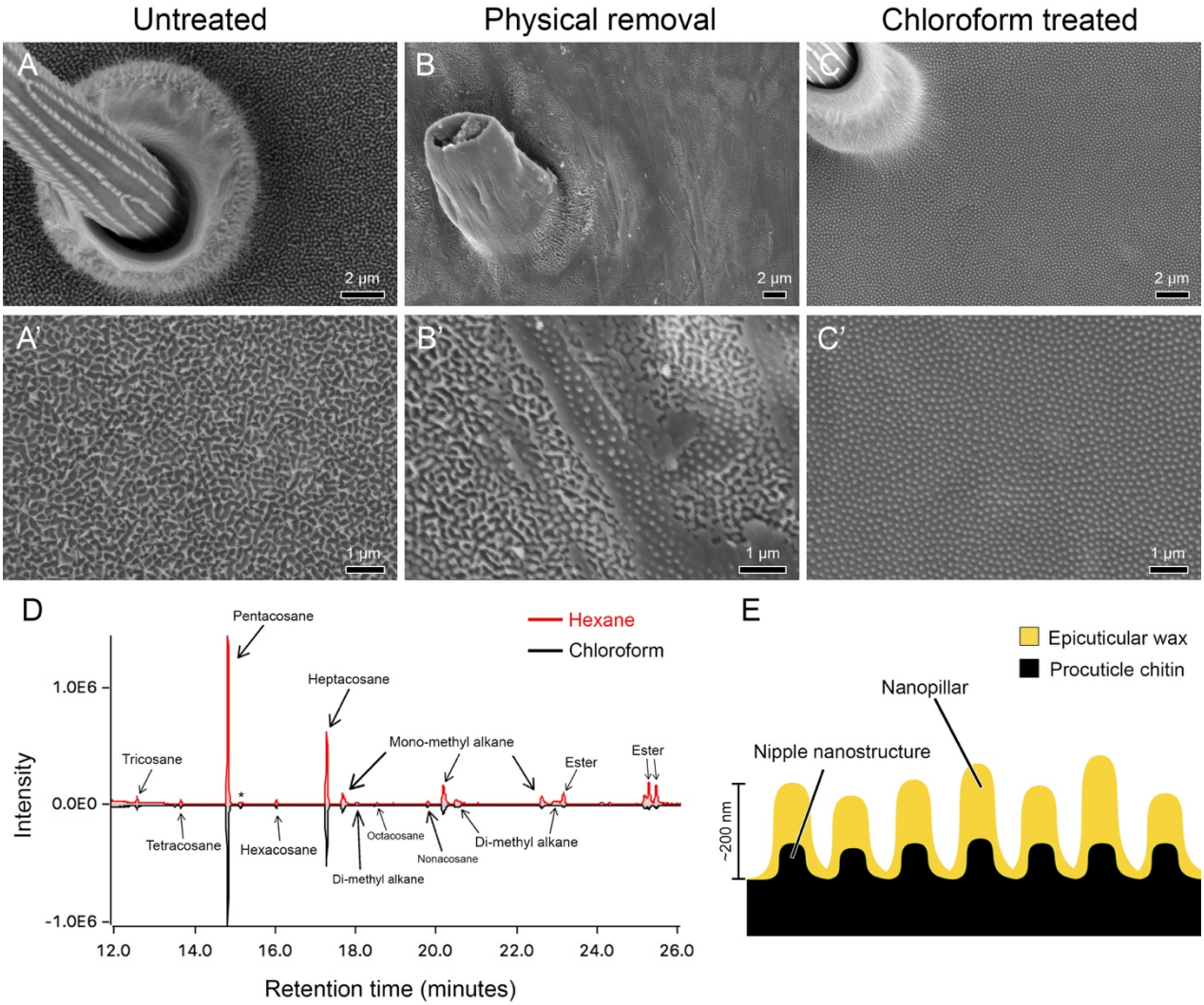

Fig. 5. Topographical organization and biochemical composition of wing surface nanostructures

Scanning electron microscopy of the transparent wing membrane surface of *Greta oto* under **(A-A')** untreated condition, highlighting the presence of irregularly arranged nanopillar structures covering the surface, **(B-B')** physical treated condition, revealing partial removal of surface nanopillars, and a lower layer of more regularly arranged nipple-like nanostructures and **(C)** chloroform treated condition, revealing complete removal of the upper layer of nanopillars, and remining lower layer of nipple-like nanostructures. Scale bars in **(A, B C)** = 2 µm, scale bars in **(A', B', C')** = 1 µm. **(D)**

368 Chromatogram of hexane-treated (top; red line) and chloroform-treated (bottom; black
369 line) clearwing extracts. X-axis shows the retention time in minutes and Y-axis shows the
370 abundance of total ion current. **(E)** Schematic of proposed wing surface membrane
371 nanostructures in *Greta oto*, composed of chitin-based procuticle and wax-based
372 epicuticle.

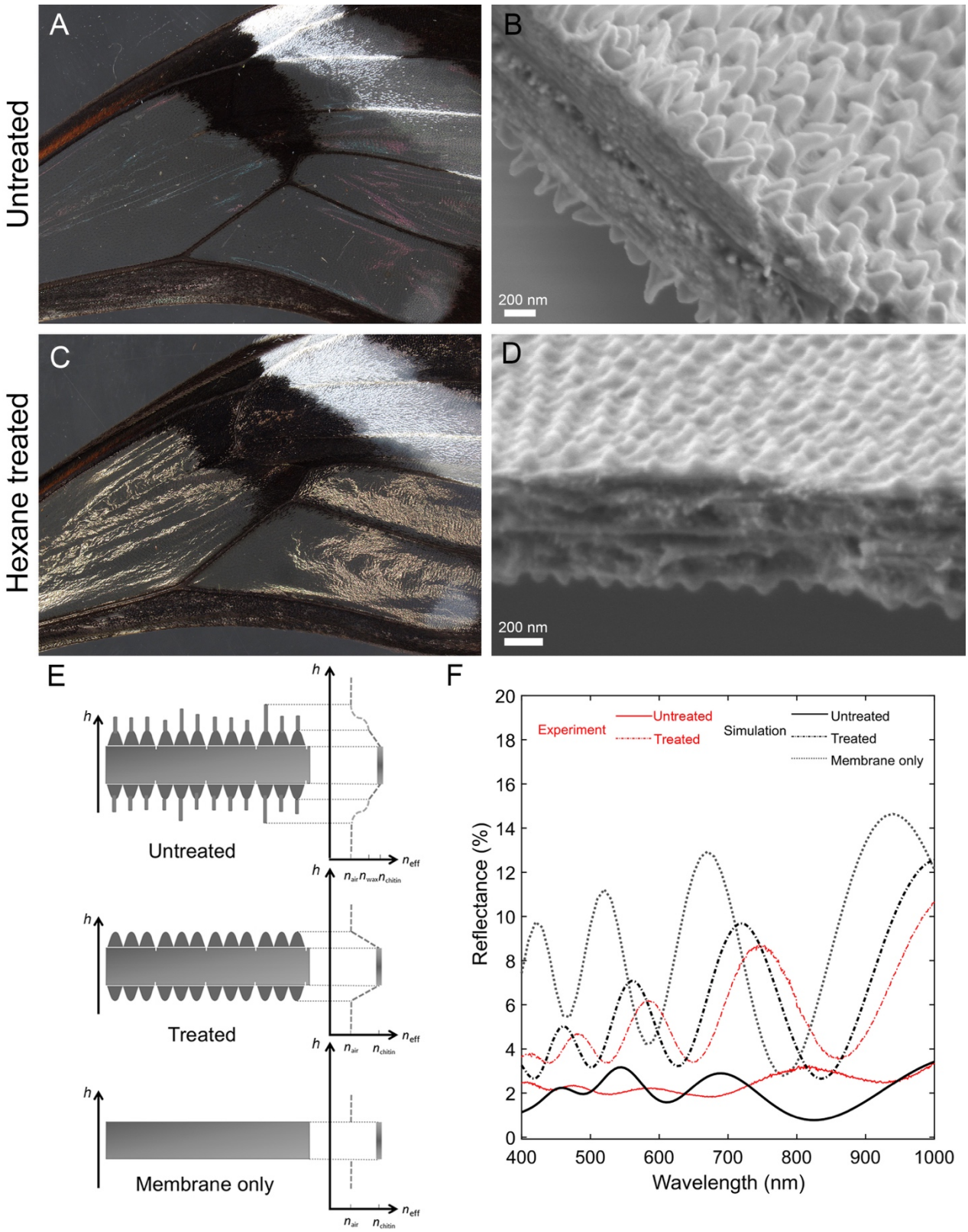

Fig. 6. Structural elements, reflectance spectra and optical modeling of anti-reflective nanostructures

Optical images and cross section scanning electron microscopy of *Greta oto* **(A, B)** untreated wings, illustrating low reflectance and the presence of nanopillars on the wing membrane surface and **(C, D)** hexane-treated wings illustrating increased reflectance and the loss of nanopillars on the wing membrane, but presence of nipple-like nanostructures on the surface. Scale bars for **(B, D)** = 200 nm. **(E)** Optical modeling of effective refractive index conditions for untreated (top), with nanopillars of variable height together with cuticle-based nipple nanostructures on the wing membrane, treated (middle) with cuticle-based nipple nanostructures on wing membrane and wing membrane without any nanostructures (bottom). Y-axis represents height *h* and X-axis represents effective refractive index condition of air (n_{air}), chitin (n_{chitin}), and wax (n_{wax}). **(F)** Representative reflectance spectra of experimental (red) and simulation data (black) for untreated wings with nanopillars on the membrane surface (solid line), hexane-treated wings with the wax-based layer of nanopillars removed (dashed line) and membrane only (dotted line).

890 **Supplementary Materials**

891 **Table S1. GC-MS relative proportions (mean ± standard deviation) of wing cuticular**
892 **compounds isolated from *Greta oto*.**

893

894 **Table S2. Spectrometry of *Greta oto* untreated and hexane treated clear wing regions**
895 **and simulated reflectance spectra.**

896

897 **Movie S1. 3D projection of developing scales in a clear wing region 48 hours after**
898 **pupal formation.** 3D projection and rotation of the same scales shown in Fig. 2F, 48
899 hours APF in a clear wing region. WGA (magenta) stains cell membranes and phalloidin
900 (green) stains F-actin and DAPI (blue) stains nuclei. Short actin filaments have
901 reorganized and formed smaller numbers of thick, regularly spaced parallel bundles just
902 under the surface of the cell membrane. Scales alternate with future forked scales
903 appearing as triangular shapes and longer future bristle-like shapes.

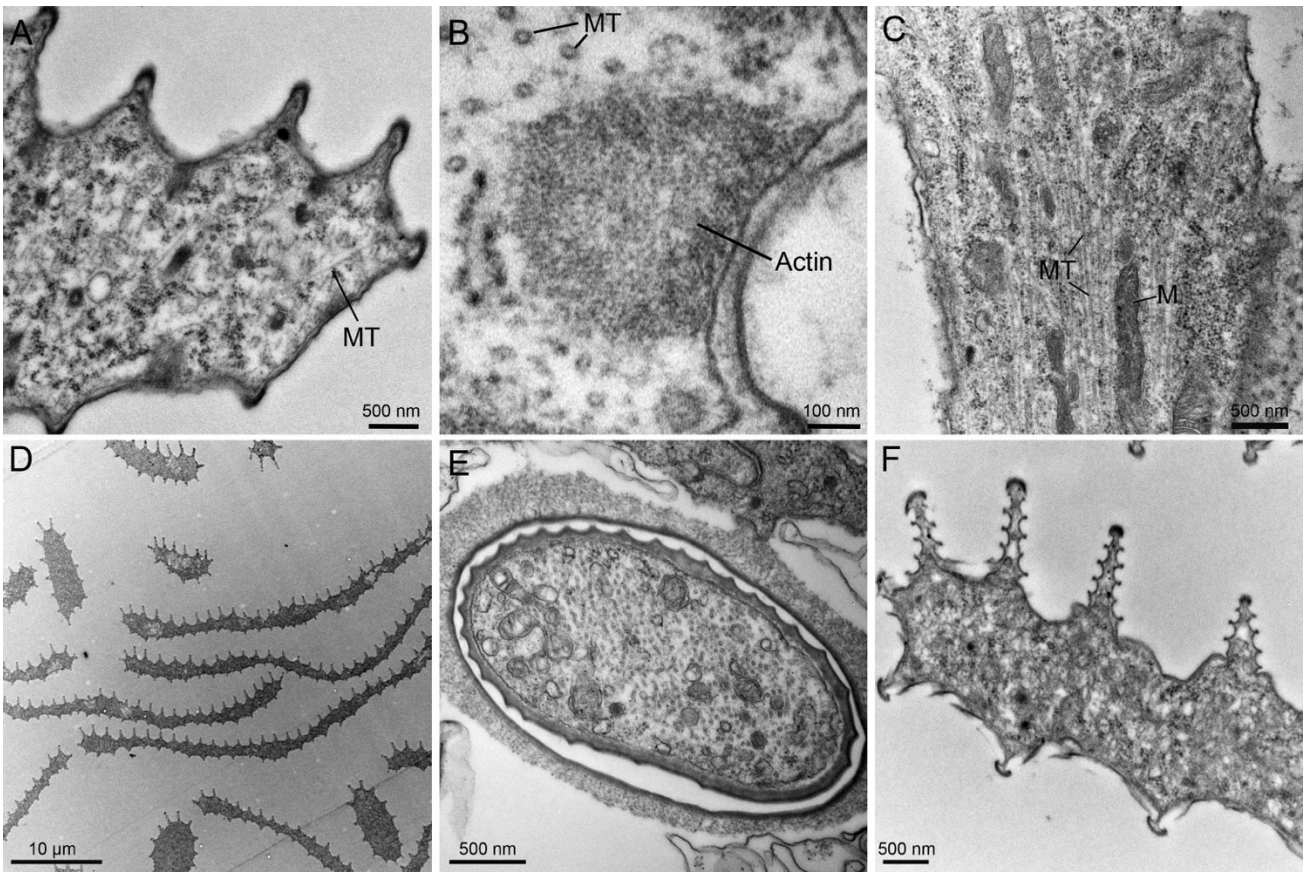

Fig. S1. TEM micrographs of scales 72 hours (top) and 120 hours (bottom) after pupal formation

(A) TEM micrograph of a developing opaque scale 72 h APF, highlighting microtubule arrangement (MT). **(B)** Thick actin bundles contain dense, hexagonally packed F-actin filaments. **(C)** Basal region of a developing scale outgrowth and socket cell. Developing scales 72 h APF contain dense populations of microtubules (MT) and numerous internal organelles, including mitochondria (M), electron dense vesicles and free single ribosomes. **(D)** Transverse section of developing scales around 120 h APF, highlighting both flat and thin, bristle-like scale morphologies. Cross section near the **(E)** base and **(F)** distal region of scales 120 h APF, showing thickened cuticle and ridge morphologies.

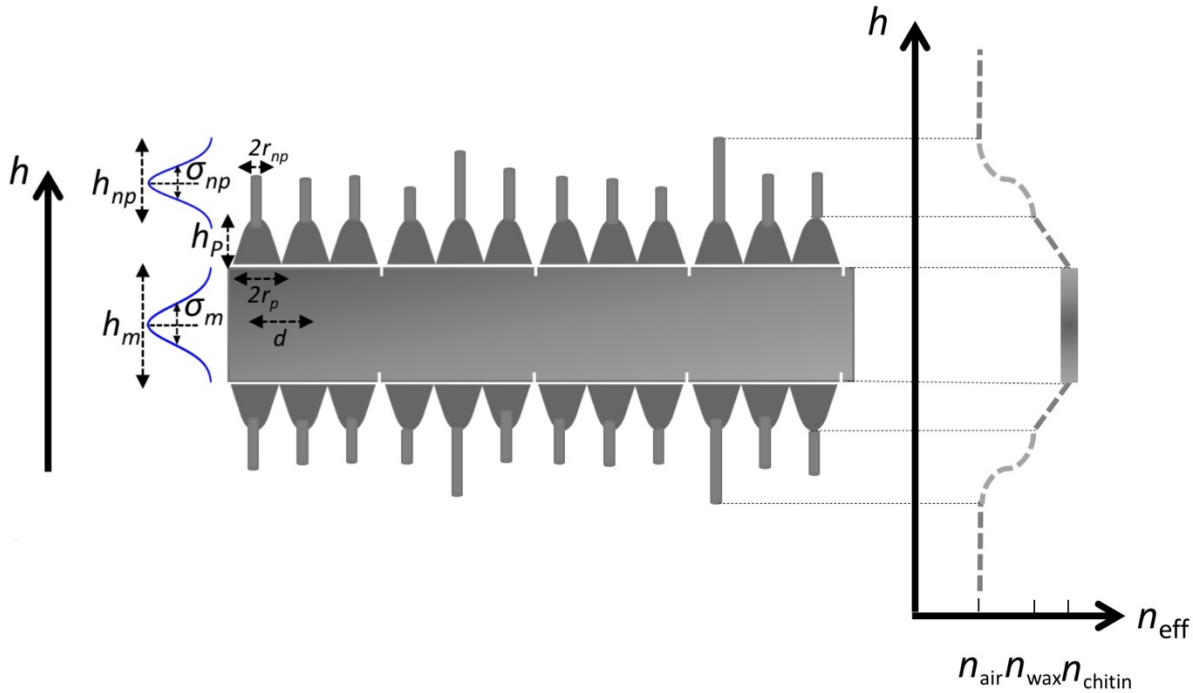

Fig. S2. Optical modeling parameters and effective refractive index condition for untreated transparent wing of *Greta oto*

Schematic representation for the optical modeling parameters of wing membrane and surface nanostructures. Average distance between two nanostructures represented as d, conical shaped cuticular nipple nanostructures height as h_p, wax-based irregular nanopillars radius as r_{np}, mean height as h_{np} and variance σ_{np}, and membrane thickness as h_m and variance σ_m. Y-axis represents height h and X-axis represents effective refractive index condition of air (n_{air}), chitin (n_{chitin}), and wax (n_{wax}).

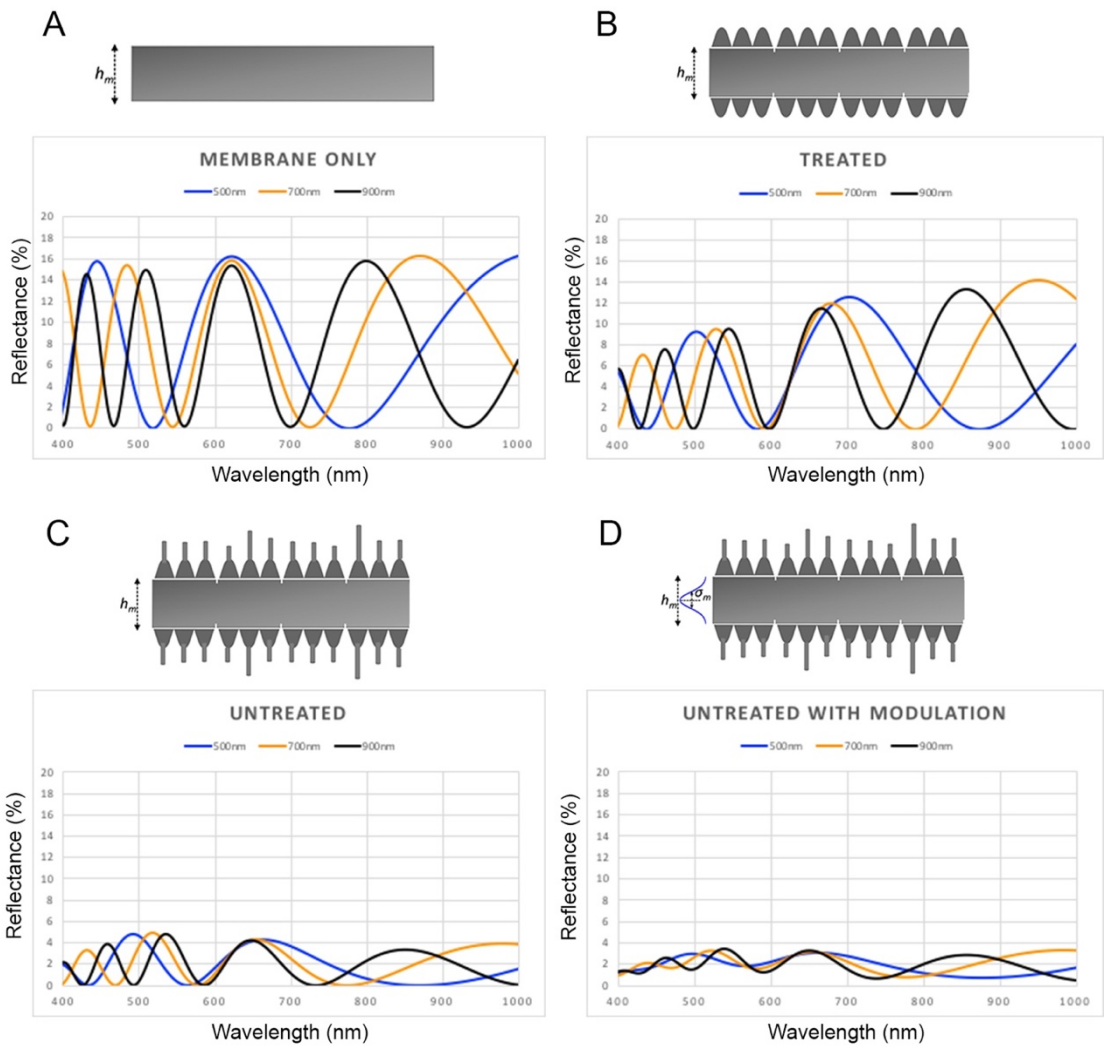

924

925 **Fig. S3. Optical simulations for mean membrane thickness and modulation of**

926 **thickness under different wing architecture models**

927 Simulation reflectance spectra of **(A)** Membrane only (lacking surface nanostructures)

928 with varying mean membrane thickness. **(B)** Treated wings (containing cuticle-based

929 nipple nanostructures but lacking wax-based irregular nanopillars) with varying mean

930 membrane thickness. **(C)** Untreated wings (containing wax-based irregular nanopillars and

931 nipple nanostructures) with varying mean membrane thickness and no modulation in

932 thickness. **(D)** Untreated wings with variable mean membrane thickness and modulation

933 of 43 nm variance in thickness.